NAZARBAYEV
UNIVERSITY

School of Engineering and Digital Sciences

Bachelor of Engineering in
Mechanical and Aerospace Engineering

Exploration of Additively Manufactured Metamaterials for Aerospace Applications

(Final Report for Capstone Project)

by

Arman Azhbagambetov
Kamila Saulenbekova

Principal Supervisor: Didier Talamona
Co Supervisor: Asma Perveen

April 2025

I. Declaration

We hereby declare that this report entitled “Exploration of Additively Manufactured Metamaterials for Aerospace Applications” is the result of our own project work except for quotations and citations that have been duly acknowledged. We also declare that it has not been previously or concurrently submitted for any other degree at Nazarbayev University.

Names: Arman Azhbagambetov, Kamila Saulenbekova

Date: April 28th, 2025

II. Acknowledgments

We would like to extend our profound appreciation to our supervising professor, Didier Talamona, for his guidance, productive feedback, and support during the adventure. His expertise and encouragement have been critical in shaping this research and helping us grow both academically and personally.

Above all, we would like to express our grateful appreciation to the laboratory assistants and senior students for their patience, technical assistance, and untiring effort in making things possible for our experiments. We would now like to express words of appreciation to Nazarbayev University for the enabling academic environment and facilities that made this research possible. Being part of this great institution is a privilege and an experience that we will always cherish.

We would like to thank each and every one of you for the contribution towards this project, which otherwise would not have happened.

Abstract

This project aimed to investigate the energy absorption capabilities of symmetrical and asymmetrical mechanical metamaterial structures fabricated from Al7075 using Selective Laser Melting (SLM) on an AM400 printer. A critical initial step involved optimizing the SLM printing parameters for Al7075, a high-strength aluminum alloy challenging to process due to its susceptibility to cracking. Parameter optimization was conducted by systematically adjusting laser power and exposure time in batches, starting from an AlSi10Mg baseline, and evaluating the resulting mechanical properties, including compressive strength, hardness, and tensile strength. The optimization process successfully improved the compressive strength of the Al7075 material. Following parameter optimization, symmetrical and asymmetrical SSR honeycomb structures were printed and subjected to compression testing to assess their energy absorption performance. The asymmetrical 30◦ SSR design demonstrated an improved energy absorption capacity compared to the symmetrical structure, although both exhibited brittle fracture behavior under compression. This study highlights the potential of structural asymmetry in enhancing energy absorption in additively manufactured Al7075 metamaterials, while also underscoring the importance of robust parameter optimization and addressing material brittleness and testing methodology limitations for high-performance applications like aircraft wing leading edges.

List of Figures:

List of Tables:

Table of contents

1. Introduction

Mechanical metamaterials represent a revolutionary class of engineered materials whose mechanical properties are dictated not by their chemical composition but by their carefully designed structural architecture. These materials are composed of repeating unit cells that determine their unique behaviors, such as negative stiffness, negative Poisson's ratio [1], and exceptional energy absorption. Advances in additive manufacturing have enabled the precise fabrication of these complex structures, though challenges like high production costs and scalability remain. Despite these limitations, mechanical metamaterials offer unparalleled versatility, allowing tailored properties that surpass conventional materials. For instance, auxetic metamaterials expand under tension, making them ideal for aerospace and biomedical applications, while nanolattices combine ultrahigh strength with lightweight characteristics for use in civil engineering and energy storage [2]. Additionally, magneto-mechanical metamaterials provide tunable stiffness for soft robotics, and truss-based lattices like the Octet Truss deliver efficient load distribution in lightweight designs [3]. The ability to manipulate mechanical properties through structural design has positioned metamaterials as transformative solutions across industries, from noise insulation and impact protection to adaptive prosthetics and high-performance aerospace components [4].

Among the diverse topologies of mechanical metamaterials, curve-based designs, such as Bézier curves and triply periodic minimal surfaces (TPMS), exhibit superior energy absorption and reduced stress concentrations due to their smooth, continuous geometries [5]. TPMS structures - including gyroids, Schwarz Diamond, and Primitive surfaces - are particularly notable for their minimal surface area and even load distribution, enhancing fatigue resistance. In contrast, truss-based lattices like the Octet Truss and Body-Centered Cubic (BCC) configurations prioritize stiffness and strength, making them suitable for structural applications. Another intriguing class is pentamode materials, which exhibit extreme compliance, enabling applications in vibration damping and acoustic wave manipulation. However, auxetic structures stand out for their negative Poisson's ratio, allowing them to expand transversely under axial tension. Re-entrant, rotating rigid unit, and chiral auxetic designs excel in energy absorption, impact resistance, and shape retention, making them invaluable for protective equipment and aerospace components.

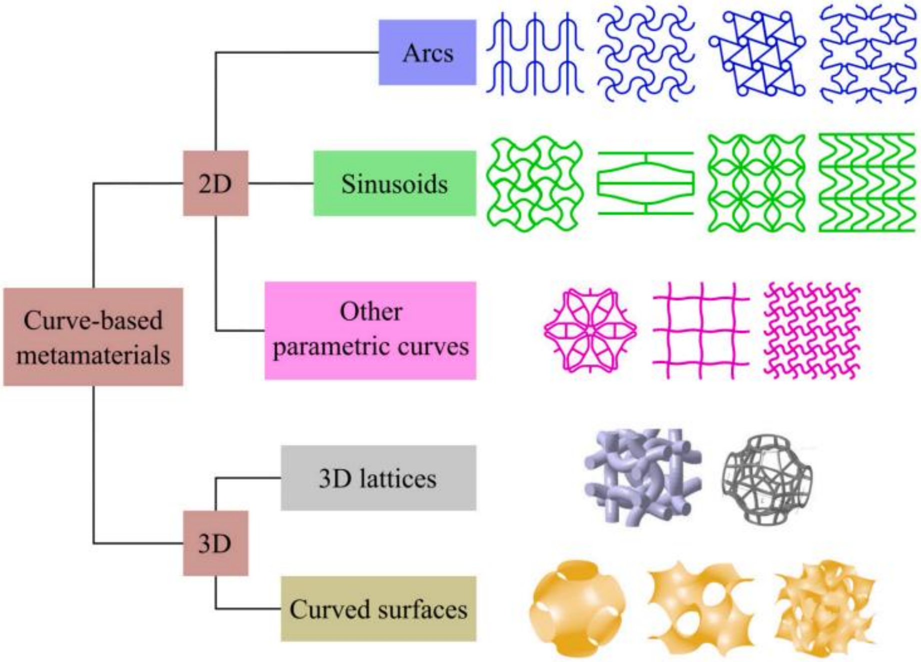

Figure 1. Types of curve-based metamaterial structures [5].

This capstone project focuses on optimizing mechanical metamaterials for the leading edge of aircraft wings, a critical area requiring enhanced energy absorption to withstand impacts and turbulence. Traditional materials often fall short in meeting these demands, as their properties are intrinsically fixed. By systematically evaluating different metamaterial designs, this study aims to identify structures with superior strength-to-weight ratios tailored for aerospace applications [6]. A key inspiration comes from Bahmanpour et al.'s work on asymmetric re-entrant auxetic honeycombs, which demonstrated significant improvements in specific energy absorption (SEA) compared to symmetric designs [7]. Their study highlighted the potential of Single Symmetry-Broken Re-entrant (SSR) and Double Symmetry-Broken Re-entrant (DSR) configurations, fabricated via fused filament fabrication, in achieving exceptional mechanical performance.

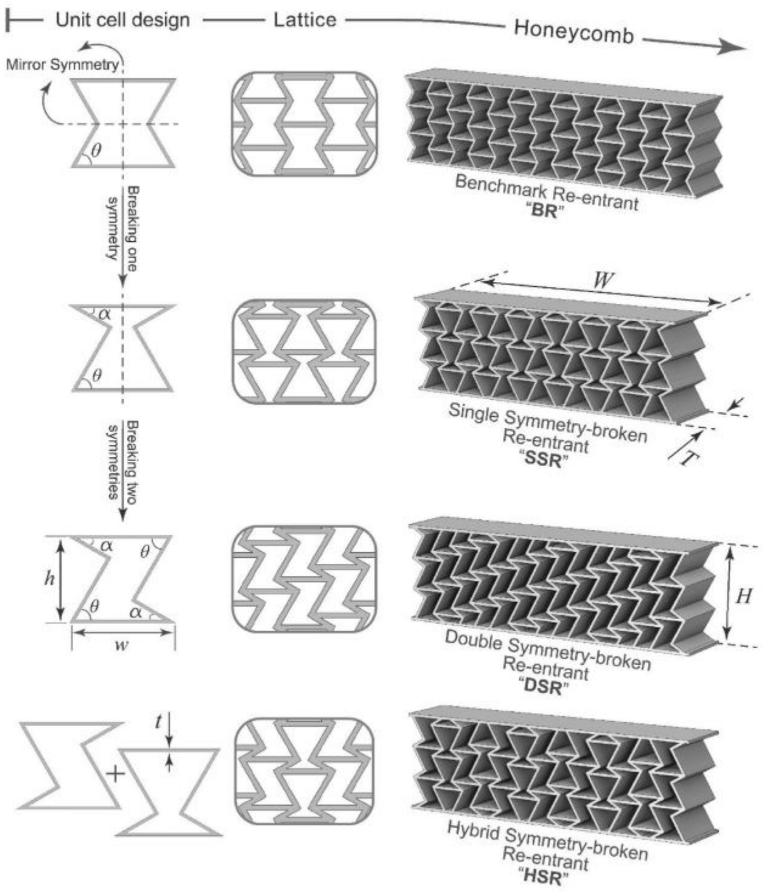

Figure 2. The structures of asymmetric auxetic honeycombs [7].

Building on this foundation, the proposed research will employ Selective Laser Melting (SLM) to manufacture SSR honeycomb structures using Al7075 alloy, a high-strength material suitable for aerospace applications. By replicating and extending Bahmanpour et al.’s methodology with advanced manufacturing and materials, this work seeks to validate the superior performance of asymmetric auxetic designs while exploring their potential in next-generation aerospace structures. The findings could pave the way for lighter, stronger, and more impact-resistant wing leading edges, ultimately enhancing aircraft safety and efficiency.

The report is structured to provide a comprehensive exploration of this research. The methodology section outlines the project plan, including design parameters, fabrication via SLM. Results from experiments will detail stress distribution, deformation patterns, and energy absorption capabilities, while the discussion will interpret these findings in the context of aerospace requirements. The conclusion will summarize key insights and propose future research directions, emphasizing the transformative potential of mechanical metamaterials in advancing engineering applications. Through this cohesive and interdisciplinary approach, the study aims to bridge the gap between theoretical design and practical implementation, unlocking new possibilities for metamaterials in high-performance systems.

Main objectives of this research is to optimise metamaterial structures for enhanced energy absorption capability for leading edge. This research proposes the use of asymmetrical honeycomb lattice and estimates its the performance on Al7075.

2. Project plan:

The project is structured to run from August 2024 to April 2025, comprising twelve sequential and overlapping tasks (Table 1, Figure 3). It begins with a comprehensive literature review, followed by the design of lattice structures, simulation studies, and the development of initial process parameters. Subsequent phases include the printing and testing of initial parameters, parameter optimization, and the testing of printed parts.

The calendar plan is illustrated using a Gantt chart, which maps the start and completion dates for each task. Some tasks, such as lattice design and simulations, overlap with the literature review to optimize time usage. Critical activities such as parameter optimization and printed parts testing span longer durations, reflecting their complexity and importance within the project timeline. A planned gap between initial printing and testing phases allows for preparation and adjustments.

The project is carefully scheduled to ensure a logical progression between tasks, maintaining continuity and minimizing idle periods. It is expected to conclude successfully by the end of April 2025, with final activities including lattice testing and the preparation of the project report.

Table 1. Calendar plan

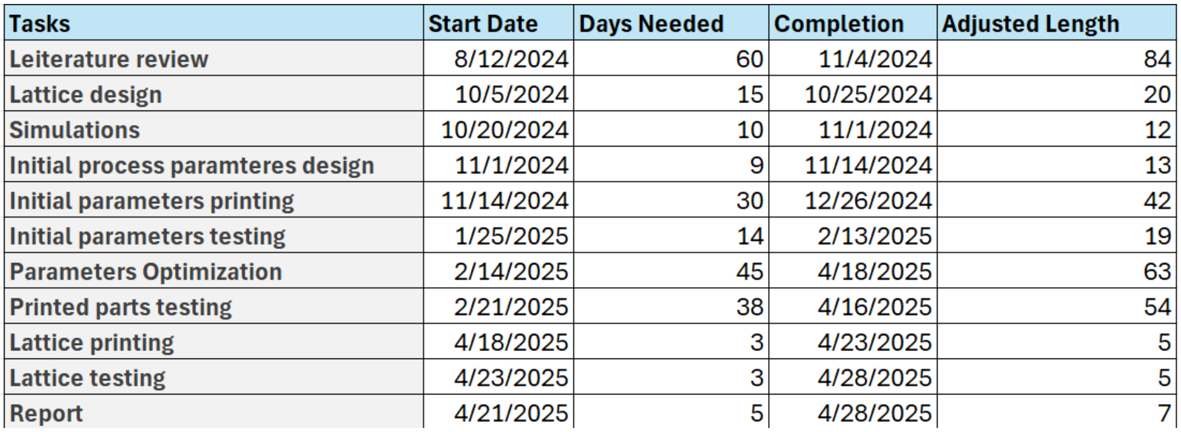

Tasks	Start Date	Days Needed	Completion	Adjusted Length
Leiterature review	8/12/2024	60	11/4/2024	84
Lattice design	10/5/2024	15	10/25/2024	20
Simulations	10/20/2024	10	11/1/2024	12
Initial process paramteres design	11/1/2024	9	11/14/2024	13
Initial parameters printing	11/14/2024	30	12/26/2024	42
Initial parameters testing	1/25/2025	14	2/13/2025	19
Parameters Optimization	2/14/2025	45	4/18/2025	63
Printed parts testing	2/21/2025	38	4/16/2025	54
Lattice printing	4/18/2025	3	4/23/2025	5
Lattice testing	4/23/2025	3	4/28/2025	5
Report	4/21/2025	5	4/28/2025	7

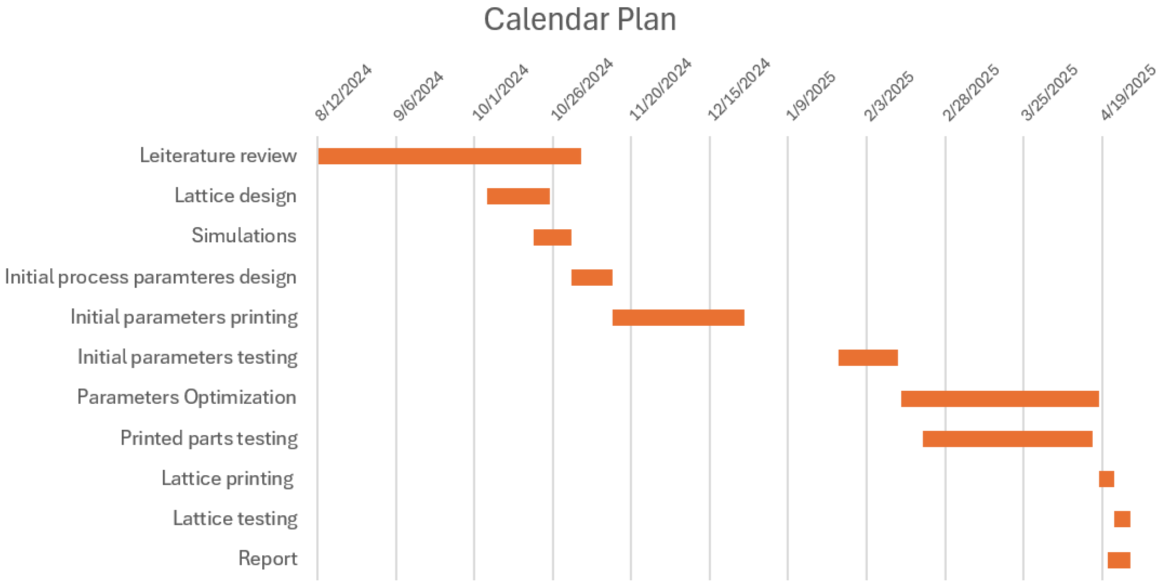

Figure 3. Calendar plan by periods graph

3. Methodology

3.1 Material: Al7075

The investigation utilizes Aluminum 7075 (Al7075) as the material selection because it represents a heat-treatable high-strength alloy based on aluminum, zinc, magnesium, and copper. Al7075 has become popular within aerospace sectors due to its exceptional mechanical properties that include substantial tensile strength along with fatigue resistance along with ductile properties. Additive manufacturing of Al7075 causes issues because the material tends to crack when hot and develop defects, leading for need to optimize its process parameters. The supplier of Aluminum alloy powder has provided information on chemical composition and particle size distribution. However, to ensure that Al7075 powder would exhibit the predicted properties, EDS and SEM were conducted. The expected ultimate compressive strength was 583 MPa, ultimate tensile 572 MPa, vickers hardness 122, and density 2.77-2.83 g/cc [8,9].

3.2 Design of asymmetric honeycomb structure

This research investigates the mechanical properties of Single Symmetry-Broken Re-entrant (SSR) honeycomb structures, which have different asymmetric elements. Two Single Symmetry-Broken Re-entrant honeycombs were designed to compare symmetric honeycombs through their use of re-entrant angles of 30° and 40°. All walls were 1 mm in thickness, the total height of each design was 21.78 mm, and the overall structure was extruded by 12.5 mm. Apart from that, there were minor differences in the total width of the structures (Table 2).

To design this lattice structure first a unit cell of honeycomb was drawn, with on internal angle fixed at 60°, and the other one varied in 30°,40°, and 60°. Then it was offset to 1mm, and repeated vertically using array function. After that, the structure was copied and rotated upside down, then it was moved to coincide with the adjusting side. One more copy was created with the initial upside position and placed on the right side. There were also two plates of 1mm height added to provide distributed stress for testing, all excess structure was trimmed (Fig. 4). CAD Models:

Three separate CAD models were designed as follows:

Table 2. Total width of each design

Structure	Width total [mm]
Symmetrical	21.16
SSR 30°	19.32
SSR 40°	19.9

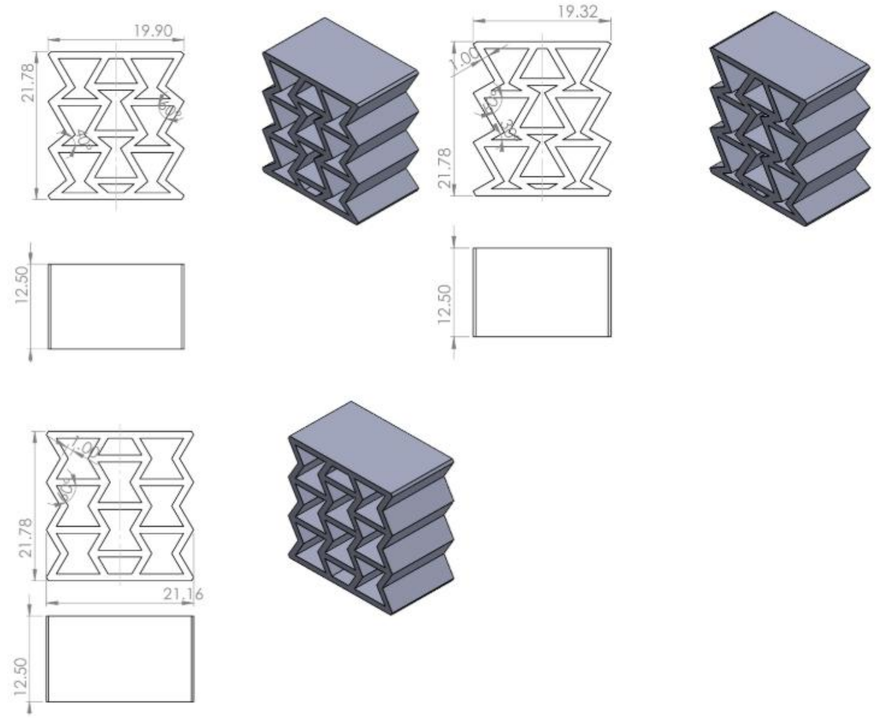

Figure 4. CAD designs of the metamaterial structures (30°SSR, 40°SSR, symmetrical)

3.3 Process parameters selection and optimization

The process of establishing suitable processing parameters for Al7075 powder on an AM400 Selective Laser Melting (SLM) printer began by leveraging existing knowledge from a similar aluminum alloy, AlSi10Mg with Laser Power of 275 W and Exposure Time of 40 μs for Hatch. Initial printing trials utilized a baseline parameter set derived from optimized AlSi10Mg parameters, serving as a starting point for exploring the Al7075 process window. Recognizing the potential differences in material behavior, a systematic approach was adopted for subsequent optimization batches. The first iteration involved increasing the laser power by 10% compared to the baseline AlSi10Mg settings, aiming to assess the impact of higher energy input on melt pool stability, density, and microstructure for Al7075. Following the evaluation of this batch, a second optimization step was conducted. In this phase, the exposure time was increased by 10% relative to the previous batch's settings, while maintaining the adjusted power level. This sequential modification of key parameters allowed for a focused investigation into their individual and combined effects on the Al7075 material's response during the SLM process, facilitating the identification of parameters leading to improved part quality and material properties.

Figure 5. AM400 Selective Laser Melting (SLM) printer

3.4 Testing of parameters

Tests of mechanical properties systematically occurred after the printed batches were finished. Multiple samples of different parameters were manufactured to achieve precise results of mechanical properties of printed Al7075 structures.

The test specimens for compression evaluation had dimensions of 6 mm diameter and 12 mm height when prepared in cylindrical shape. The aspect ratio (1:2) was maintained to prevent buckling, so tests could be performed accurately to determine ultimate compressive strength under static loading. The compressive tests became essential for determining how well the material performs under compressive stress since energy-absorbing structures need this capability for both impact and crushing scenarios.

Standard smooth round bar specimens underwent tensile testing through measurement of their 25 mm gauge length. Tensile testing procedures helped determine both ultimate tensile strength (UTS) values and material ductility levels which matter highly for aerospace integrity assessments since structures need to succeed under tension alongside compression loading conditions.

A testing process of hardness used rectangular specimens with dimensions of 10 × 10 × 3 mm. Special attention was given to surface polishing of the samples for uniform testing standards. Repetitive Vickers hardness tests performed on each specimen utilized various indentations as a way to mitigate the effects of heterogeneity which may occur because of additive manufacturing. To conduct this test the dwell time was set to 12sec and force of 100g was applied. The average results from hardness tests of multiple points were used to precisely evaluate how resistant the printed material was at local points.

To assess the internal structural and chemical homogeneous analysis cubes with dimensions of 10 × 10 × 3 mm were printed perpendicular to the build platform. The combination of Scanning Electron Microscopy (SEM) allowed to view surface features and search for porosity and verify how different layers united. Also, by multiple steps of polishing and etching, it was possible to observe a microstructure and evaluate defects. Prior to polishing samples were inserted into polymer compound and baked to automate the polishing process. Polishing consisted of four steps, strating with planar grinding with P320 sandpaper and water, then Beta polishing medium was used for another 5 min with 9mkm of Dia complete poly supply. The last two steps of polishing used sigma and omega medium with 3 and 1mkm of liquid. Finally, to etch the samples Keller reagent was used, that consisted of concentrated sulfuric acid (H_2SO_4), glacial acetic acid (CH_3COOH), and ferric chloride ($FeCl_3$). Samples were etched for different durations from 5 seconds to 1 minute. At last, after cleaning them with ethanol, SEM was performed.

EDS analysis was needed to verify that the SLM process did not cause meaningful compositional segregation or contamination through evaluations of elemental distribution across the parts.

The analysis of scanning electron microscopy (SEM) images was done through the ImageJ software execution. The measurement process started with calibrating the images after researchers used scale bars inside micrographs to maintain accurate measurement of particles and defects. After calibration the images were changed to 8-bit grayscale format then a threshold setting method was applied to separate defects from the background. The ImageJ software used "Analyze Particles" functionality to measure numbers of defects while obtaining their combined area size as well as average measurements and field defect coverage percentage. The examination was conducted at four different magnification levels (7500x, 3300x, 300x, and 450x) for detecting how defects spread and altered in size based on the observation scale. All evaluated images received similar threshold constraints that helped achieve uniformity.

3.5 Testing of the energy absorption capability of asymmetric structures

To meet the main objective of this research, compression tests were conducted on three symmetrical honeycomb structures and the same amount of asymmetrical Single Symmetry-Broken Re-entrant (SSR) honeycombs of 30° and 40° re-entrant angles for energy absorption evaluation. These tests examined the relationship between structural asymmetry and energy absorption under compressive loading because leading edges in aircraft wings demand high impact resistance.

The tests applied quasi-static compression strains at controlled rates of 1 mm/min during which each sample underwent uniform loading conditions. The tests produced detailed stress-strain plot information for each experimental sample. From the plot it was possible to determine Energy Absorption through area integration under the stress-strain curve until densification began.

The honeycomb symmetrical structure acted as a reference point to compare it against the 30° and 40° SSR designs. The 30° SSR design was expected to achieve maximum energy dissipation. The research evaluated different designs to identify the best structural asymmetry level that maximizes mechanical efficiency.

4. Results

4.1 Printed Testing Samples

The Al7075 honeycomb-structured metamaterials were fabricated using selective laser melting (SLM) with optimized printing parameters (Figure 6). Three distinct honeycomb configurations were manufactured: (1) symmetrical honeycomb with uniform hexagonal cells, (2) 30° asymmetrical honeycomb featuring angled cell walls for progressive collapse, and (3) 40° asymmetrical honeycomb with a more aggressive wall offset for enhanced energy dissipation.

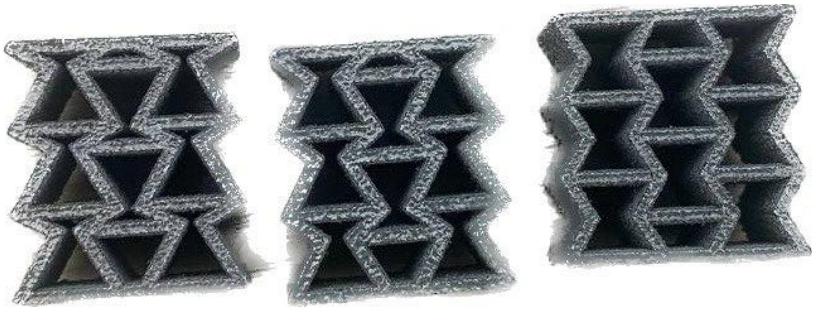

Figure 6. 30∘,40∘,symmetrical structures

For mechanical testing, four specimen types were produced:

Compression samples: Cylindrical specimens (6 mm diameter × 12 mm height).

- Tensile samples: Standard tensile specimens with a 25 mm gauge length.
- Hardness samples: 10 × 10 × 3 mm polished cubes for Vickers hardness testing.
- Microstructural samples: 10 × 10 × 3 mm blocks sectioned parallel and perpendicular to the build direction for SEM/EDS analysis.

Figure 7. Tensile, Compression, Hardness, Microstructure testing samples

4.2 Compression Test Results

The compressive behavior of the Al7075 was evaluated using cylindrical specimens with a diameter of 6 mm and a height of 12 mm, maintaining a diameter-to-height (d/h) ratio of 1:2. The tests were conducted under quasi-static loading conditions to determine the ultimate compressive strength (UCS) of each batch.

First Batch: The specimens exhibited an ultimate compressive strength of 284 MPa, representing the lowest performance among the three batches. This could be attributed to potential inconsistencies in the additive manufacturing process, such as incomplete fusion or porosity within the structure.

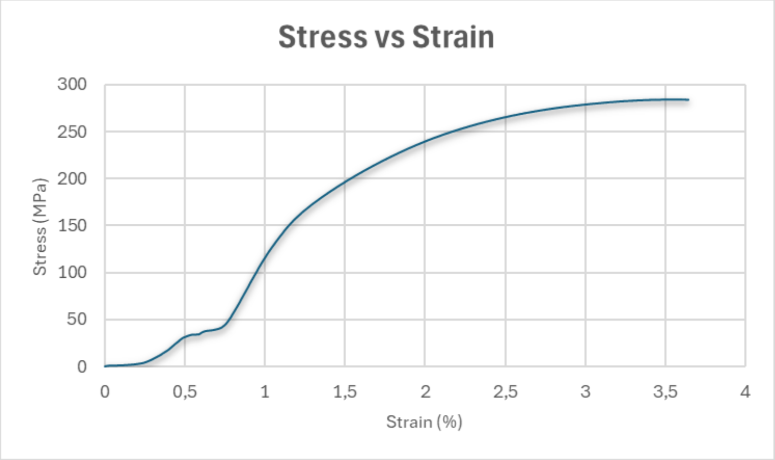

Figure 8. Stress vs Strain curve (Batch 1)

Second Batch: The compressive strength improved significantly to 320 MPa, suggesting better structural integrity, possibly due to optimized printing parameters or reduced internal defects.

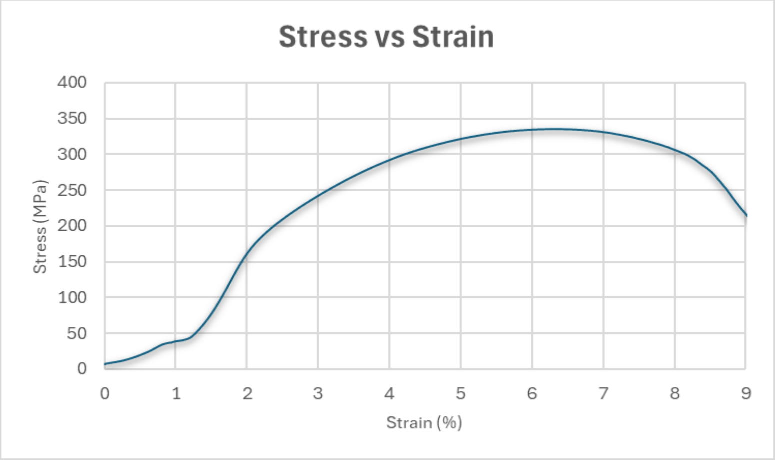

Figure 9. Stress vs Strain curve (Batch 2)

Third Batch: The highest compressive strength was recorded at 408 MPa, indicating superior mechanical performance. This enhancement may result from refined microstructure, improved layer bonding, or geometric modifications in the honeycomb design.

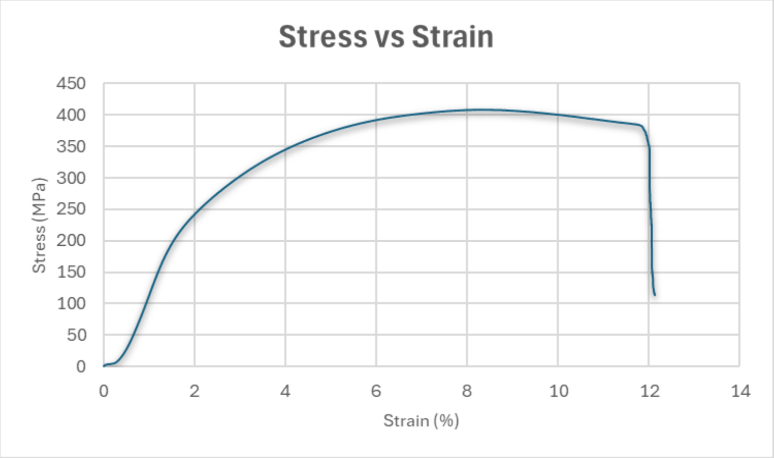

Figure 10. Stress vs Strain curve (Batch 3)

4.3 Hardness Test Results

Vickers hardness (HV) measurements were performed on rectangular specimens (10×10×3 mm) to assess localized mechanical resistance. Multiple indentations were made per sample to account for material heterogeneity, and averages were computed to ensure reliability.

First Batch Hardness Analysis

Sample 1: Hardness values ranged from 143.98 HV to 151.02 HV, with an average of 147.59 HV. The relatively tight distribution suggests uniform material properties.

Sample 2: Measurements showed a broader range (144.42 HV to 202.12 HV). The outlier (202.12 HV) was likely caused by a nearby void, which can artificially increase hardness due to constrained indentation deformation. Excluding this outlier, the average was 147.42 HV, consistent with Sample 1.

Sample 3: Greater variability was observed (120.78 HV to 152.65 HV), averaging 135.77 HV. The lower hardness in some regions may indicate microstructural defects, such as porosity or residual stresses from fabrication.

Second Batch Hardness Analysis

Sample 1: Hardness values ranged from 114.65 HV to 143.65 HV, with an average of 130.28 HV. The slightly lower hardness compared to Batch 1 may suggest differences in cooling rates or grain structure.

Sample 2: A wider scatter was observed (105.71 HV to 152.16 HV), with an average of 127 HV. The presence of lower hardness values (near 105 HV) could indicate softer regions due to insufficient melting or inhomogeneous powder distribution during printing.

Third Batch Hardness Analysis

Sample 1: Hardness ranged from 100.25 HV to 136.62 HV, averaging 116.8 HV, the lowest among all batches.

Sample 2: Slightly higher values (104.49 HV to 135.26 HV) were recorded, with an average of 121.46 HV.

4.4 Tensile Test Results

Uniaxial tensile tests were conducted to evaluate the ultimate tensile strength (UTS) of the Al7075. The results revealed distinct differences in tensile performance across the three batches:

First Batch: Demonstrated an ultimate tensile strength of 94 MPa, establishing the baseline performance for the printed structures.

Second Batch: Showed marginally lower tensile strength at 93 MPa, suggesting minimal variation in tensile properties despite improvements in compressive strength.

Third Batch: Recorded the lowest tensile strength at 90 MPa, indicating a potential trade-off between compressive and tensile performance.

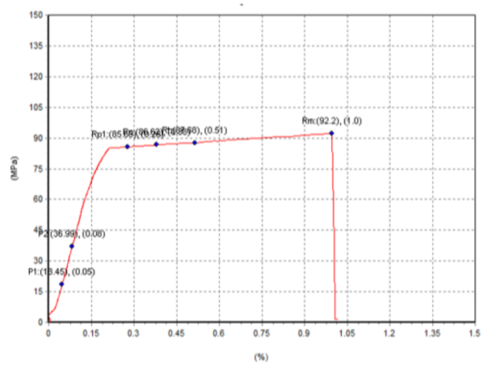

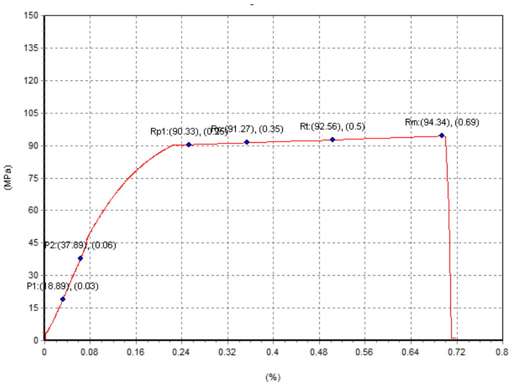

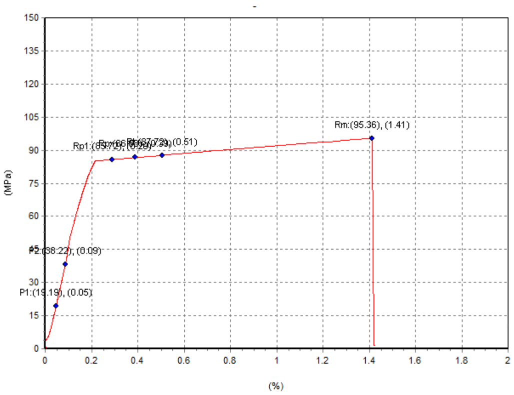

Figure 11. Stress vs Strain curve of 3 batches

4.5 Scanning Electron Microscopy (SEM) and EDS

4.5.1. Powder analysis

The magnification used (450×) demonstrates the smooth surfaces of many particles, although some degree of surface texture and satellite particles (smaller particles attached to larger ones) can be observed. The scanned particles display dimension ranges from several microns up to greater than 30µm according to accepted size parameters for SLM feedstock materials. Several particles expose small imperfections on their surfaces including pores combined with shallow craters because of gas capture during atomization (Figure 12).

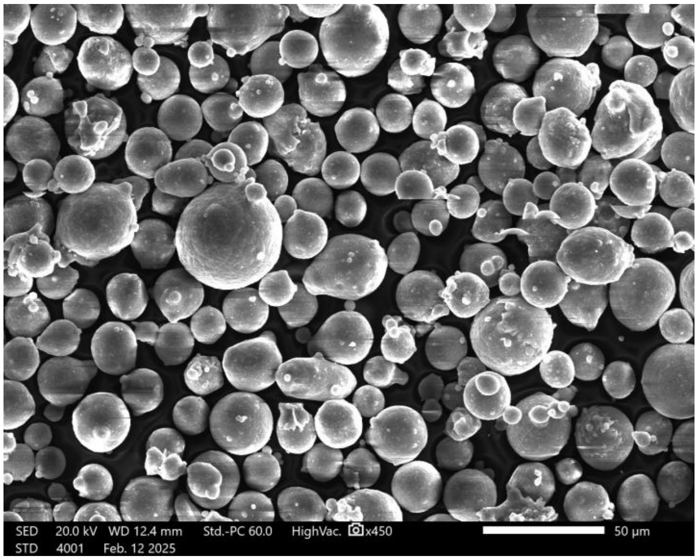

Figure 12. SEM of Al7075 powder

According to Table 3, the analyzed aluminum (Al) concentration reached 91.1% matching the balance composition yet showing below the standard level of ~92–93% found in Al7075. The tested portion of copper (Cu) content (2.37%) exceeded the permissible range of 1.2–2.0% which might result from enrichment occurring during atomization procedures or powder preparation steps.

A lack of magnesium (Mg) at 1.58% created concerns for the mechanical qualities because it went beneath the required 2.1–2.9% range specifically for Al7075. Analysis of the zinc content (4.52%) showed below-normal results regarding the specification (5.1–6.1%). The maximum and minimum thresholds for Silicon (Si), iron (Fe), chromium (Cr) and titanium (Ti) levels were met even though small variations emerged in the analysis. Manganese (Mn) cannot be detected (nd) in the tested sample since the specification allows up to 0.3%.

The tested powder deviates from specifications in Cu, Mg and Zn contents thus influencing the final mechanical properties during printed part performance analysis.

When comparing the chemical compositions of the Al7075 powder and the printed sample, several small but notable differences are observed (Table y). The aluminum (Al) content remains essentially unchanged, with 91.1 wt% in the powder and 91.0 wt% in the printed sample, indicating good retention of the base metal during the printing process. The silicon (Si) content shows a significant increase, rising from 0.11 wt% in the powder to 0.41 wt% in the printed sample. This suggests possible contamination during printing or slight enrichment due to selective evaporation or oxidation of other elements. The iron (Fe) concentration also increases, from 0.0625 wt% in the powder to 0.12 wt% in the printed sample, which may be attributed to slight contamination from the printing environment or equipment. Copper (Cu) shows a very minor decrease from 2.37 wt% in the powder to 2.3 wt% in the printed sample, indicating good stability of this element during processing. For manganese (Mn), the powder analysis indicated "nd" (not detected), while the printed sample shows a detectable amount of 0.023 wt%. This low Mn content is still within the specification limits, but its appearance suggests improved detection sensitivity or minor segregation during printing. Magnesium (Mg) content increased slightly from 1.58 wt% in the powder to 1.9 wt% in the printed sample. This is a positive observation as Mg often evaporates during high-temperature processes, so an increase suggests either enrichment or measurement variability. Chromium (Cr) content remains almost constant, with 0.215 wt% in the powder and 0.22 wt% in the printed sample, reflecting good compositional stability for this element. Zinc (Zn) shows a noticeable decrease, dropping from 4.52 wt% in the powder to 4.1 wt% in the printed sample. Since Zn is volatile at elevated temperatures, this decrease is expected and consistent with material behavior during thermal processing. Finally, titanium (Ti) content is slightly reduced from 0.047 wt% in the powder to 0.013 wt% in the printed sample, although both values are quite low and within acceptable trace levels.

Table 3. Chemical composition of Al7075 (EDS results)

Comp. (Wt. %)	Al	Si	Fe	Cu	Mn	Mg	Cr	Zn	Ti
Spec.	bal	<0.4	<0.5	1.2-2	<0.3	2.1-2.9	0.18-0.28	5.1-6.1	<0.4
Supplier	bal	0.05	0.07	1.61	0.01	2.54	0.21	5.91	0.01
Powder	91.1	0.11	0.0625	2.37	nd	1.58	0.215	4.52	0.047
Printed sample	91.0	0.41	0.12	2.3	0.023	1.9	0.22	4.1	0.013

4.5.2. Printed sample analysis

Microstructure Observations

General Features:

A polycrystalline or multiple-phase structure combined with observable grain divisions results from the microstructure together with distinct phase elements. Various parts of the material contain either tiny features measuring between 1 and 2 micrometers or larger features that amount to roughly 5 micrometers in size.

Defects Identified:

Small dark spots or voids as seen in 5 µm-scale images indicate porosity formation probably because of incomplete sintering combined with gas entrapment and etching artifacts. Linear streaks and branched fragments representing microcracks probably stem from mechanical pressure and thermal fluctuations and specimen preparation methods. The presence of bright or dark particles at 2 µm size possibly indicates non-metallic inclusions together with precipitates and contamination entities (Figure 13). Surface Roughness together with Scratches causes irregular topography due to both polishing defects and local deformation events.

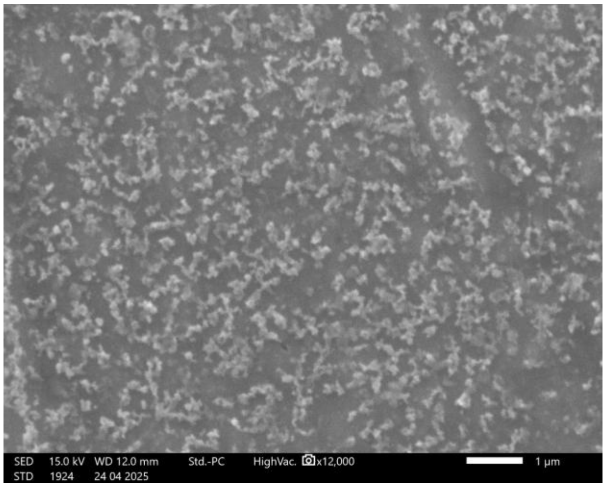

Figure 13. Precipitation (magnification 12000x)

Common structural imperfections like both porosity and cracks and inclusions appear within this microstructure because they affect mechanical characteristics such as strength and ductility. Additional tests including EDS and increased magnification, would help determine what these elements are along with their origins.

The ImageJ particle analysis reveals quantitative information about defect characteristics at different magnification levels ranging from 7500× to 300× and 450×. The particle analysis of ImageJ captured six important measurements which included Count (defect number), Total Area (occupying area), Average Size (single defect size), %Area (defect coverage) as well as Mean (gray value) and Magnification Level.

At 7500× magnification, 3290 defects were identified. These defects appear in an area of merely 1.47 units while having an exceptionally tiny average dimension of 4.47×10^{-4} units. The defects occupy 0.677% of the total image area measurement. The measurement value of 255 represents the defects' high brightness level against the background which optimizes their visibility.

The 3300× magnification produces 1661 detections of defects which occupy 2.866 units of total space. A slight area expansion of defects leads to 2.866 units while their typical size grows to 0.002 units. Among all image areas the affected percentage stands at 0.249% while defect sizes in this sample are slightly bigger than 7500× magnification.

A total of 1167 defects are detected at 300× magnification however the measured area occupation amounts to 323.667 units. The average defect sizes expand greatly to reach 0.277

units. Defects appear similar in size and spacing across all magnification levels even though the total counted defects decrease since 300× matches 0.242% of the area just like 7500×.

A total of 14,341 defects appear at 450× magnification which results in the maximum defect count. The whole defect space occupies 107.932 units while each individual defect measures an average of 0.008 units in size. The total percentage of defects in the area was found to be 0.178% at 450× magnification becoming the lowest percentage reported within the study.

Image sensitivity increases along with magnification because smaller and finer defects become detectable leading to enlarged appearance of surface defects at lower magnification levels. Surface defect monitoring in the observed field is shown by the direct reading of %Area which indicates limited coverage of defects that stays below 1% at every magnification level. The high mean gray value (255) measures that demonstrate defects appear distinguished from the background throughout the analysis process.

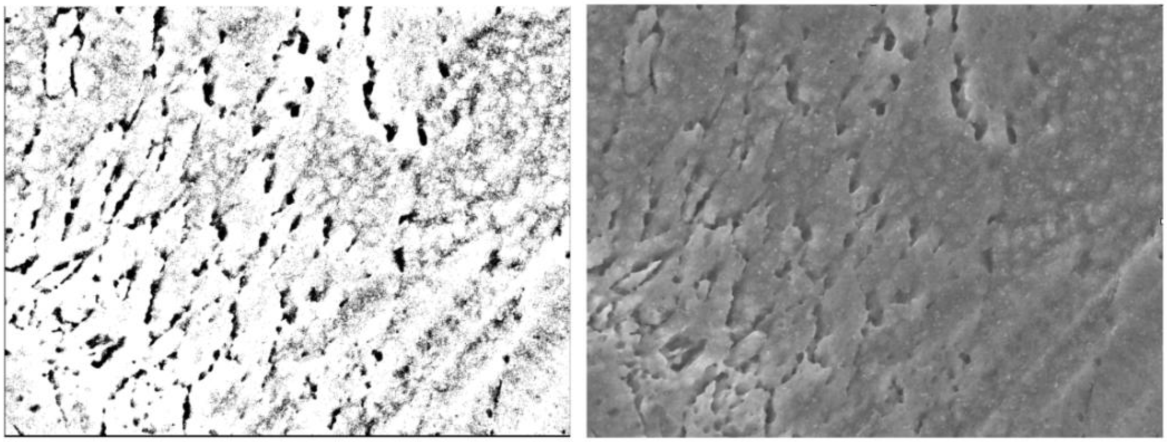

Figure 14. Magnification 3300x Sem and ImageJ

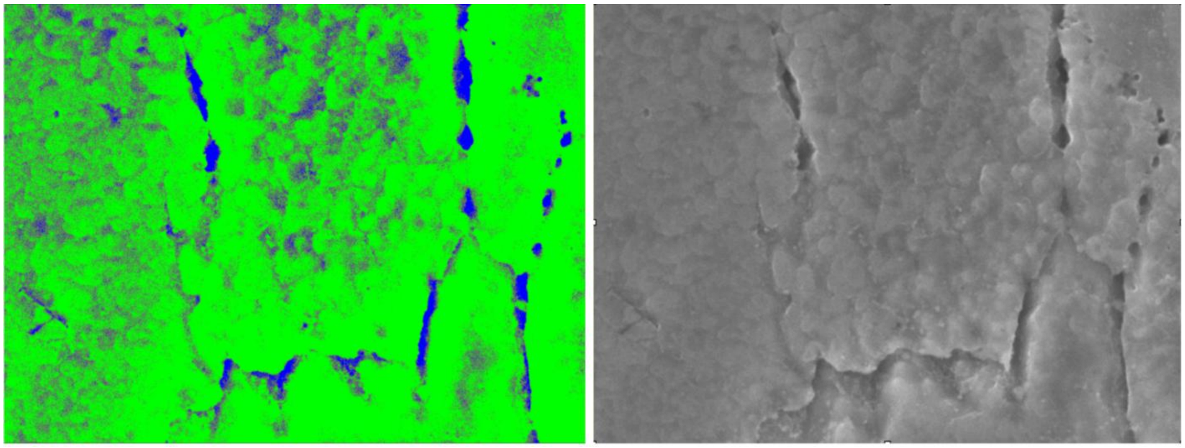

Figure 15. Magnification 7500x Sem and ImageJ

4.6 Energy Absorption Performance

Energy absorption was evaluated by comparing symmetrical and 30° asymmetrical honeycomb structures under compressive loading.

Symmetrical Honeycomb: Absorbed 39.617 J/m³, demonstrating baseline performance. The uniform cell structure likely led to predictable, but less efficient, buckling behavior.

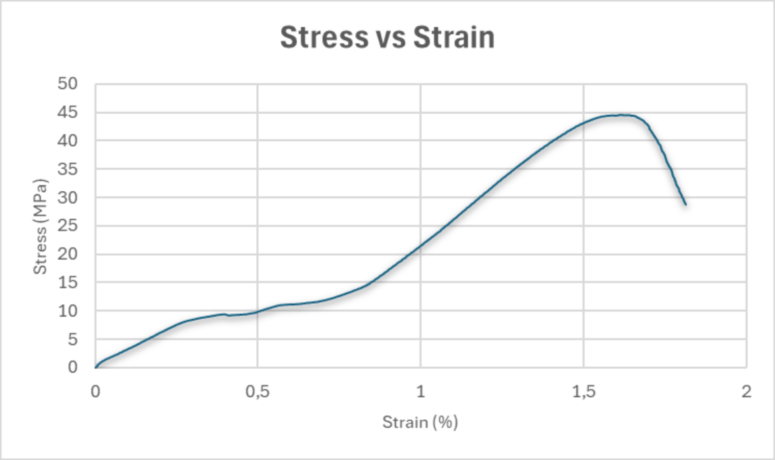

Figure 16. Stress vs Strain curve (Symmetrical)

Asymmetrical Honeycomb (30°): Exhibited 43.036 J/m³ absorption, a 8 % improvement over the symmetrical design.

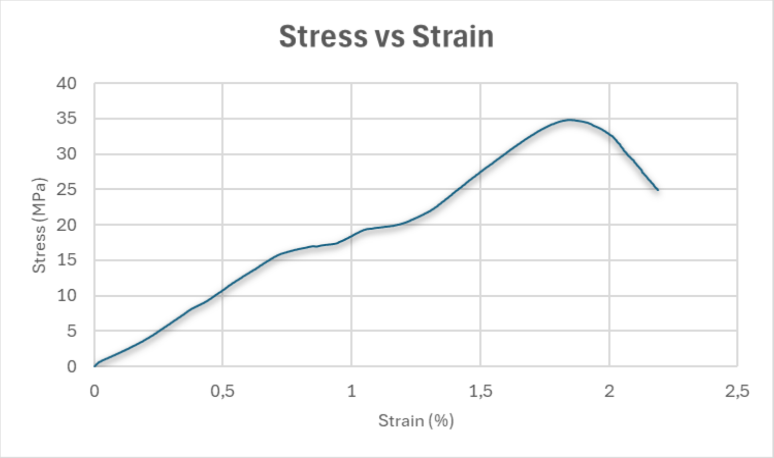

Figure 17. Stress vs Strain curve (Asymmetrical)

5. Discussion

The main aim of this project was to compare the energy absorption properties of printed symmetrical and asymmetrical structures. To achieve this, a critical initial step involved optimizing the printing parameters for Al7075 specimens fabricated on an AM400 printer, using an AlSi10Mg baseline as a starting point. Successfully fabricating complex mechanical metamaterial structures, such as the re-entrant auxetic honeycombs explored here, using Al7075 via SLM presents significant challenges, including the material's susceptibility to hot cracking. Establishing robust processing parameters was therefore essential to produce dense, defect-free material that could serve as the building block for these architecturally driven materials whose macroscopic properties are dictated by their intricate structural design rather than solely by material composition.

The increase in compressive strength observed from the first batch (baseline AlSi10Mg parameters, 284 MPa) to the second (+10% power, 320 MPa) and subsequently to the third (+10% exposure time, 408 MPa) aligns strongly with the theoretical understanding of energy density in SLM [10]. Energy density, a critical process parameter, is fundamentally the amount of laser energy delivered per unit volume of powder [11]. It can be calculated using various formulas, often involving laser power (P), scan speed (v), hatch spacing (h), and layer thickness (t), such as $E=P/(v \cdot h \cdot t)$ [12]. Increasing either laser power or exposure time (which is inversely related to scan speed for a fixed scan length) directly increases the energy density. A higher energy density generally leads to more complete melting of the metal powder particles, promoting better wetting and fusion between adjacent scan tracks and successive layers [13]. This results in a more homogeneous melt pool, reduced viscosity, and improved flow, which helps to minimize the formation of defects such as lack-of-fusion porosity and keyhole porosity. These types of porosity act as stress concentrators and significantly reduce the load-bearing capacity of the material under compression [14]. The substantial improvement in compressive strength in the third batch, where both increased power and exposure time were applied, suggests that this combined adjustment achieved a more optimal energy input for Al7075, effectively reducing internal defects and promoting a denser, more structurally sound material capable of withstanding higher compressive loads before yielding or fracturing. The inherent nature of compressive loading, which tends to close rather than open internal voids and cracks, makes it particularly sensitive to improvements in material density and fusion quality.

The hardness test results, while showing some variability within batches, generally presented a less straightforward trend compared to compressive strength. The first batch exhibited the highest average hardness, with subsequent batches showing slightly lower or comparable values. Vickers hardness (HV) is a measure of a material's resistance to plastic deformation under indentation, which is influenced by factors such as grain size, solid solution strengthening, and precipitation hardening. The observed variability within batches, particularly the outlier in the first batch and the broader scatter in the second, could be attributed to microstructural heterogeneity inherent in the additive manufacturing process [15]. Rapid solidification rates in SLM can lead to fine-grained structures and non-equilibrium phases [16]. Localized variations in cooling rates across the build plate or within a single layer can influence grain size and the kinetics of precipitation of strengthening phases like MgZn2 in Al7075 [17]. Defects such as voids (as suggested by the outlier in Batch 1, where the indenter likely hit near a pore, artificially increasing the measured hardness due to constraint) and variations in the distribution of precipitates can also significantly influence local hardness measurements [18]. While increased energy density can reduce porosity, it can also affect the thermal history and solidification path, potentially leading to changes in grain structure (e.g., grain growth at very high energy densities) and the size and distribution of precipitates [19]. The EDS analysis revealing deviations in key alloying elements (lower

Mg and Zn, higher Cu) from the standard Al7075 composition in the raw powder feedstock is a critical factor here. These compositional variations would directly impact the volume fraction, size, and distribution of strengthening precipitates, thus influencing the overall mechanical properties, including hardness, regardless of parameter optimization [20]. A lower content of Mg and Zn, essential for forming the primary strengthening precipitate MgZn2, would inherently limit the potential for precipitation hardening, potentially explaining the observed hardness values which may be lower than expected for fully optimized and heat-treated wrought Al7075.

The tensile test results consistently showed relatively low ultimate tensile strength (UTS) values across all three batches (94 MPa, 93 MPa, and 90 MPa, respectively), with a slight decrease as parameters were adjusted for improved compression. This seemingly counterintuitive result, where increased energy density led to higher compressive strength but not tensile strength, warrants careful consideration. Tensile strength is highly sensitive to defects such as porosity, lack of fusion, and microcracks, as tensile stress tends to open and propagate these flaws [21]. The observation that tensile specimen fractures occurred near the fixed position (grips) rather than in the middle of the gauge section is a crucial piece of information. In an ideal tensile test, fracture initiates and propagates from the point of maximum stress concentration, which should be within the uniformly stressed gauge section. Fracture occurring at or near the grips strongly suggests that stress concentrations introduced by the gripping mechanism, potential misalignment during testing, or localized weaknesses in the specimen near the grip area were the dominant factors leading to failure, rather than the intrinsic tensile strength of the material in the gauge section. These localized weaknesses could be due to damage from support structure removal, surface finish irregularities in the grip area, or a higher concentration of defects in regions influenced by the build plate or support structures during printing [22]. Therefore, the recorded UTS values may not accurately represent the true tensile capability of the Al7075 material produced with these parameters. The low recorded values could be an artifact of the testing methodology or specimen preparation rather than solely a consequence of the printing parameters themselves. The brittle fracture behavior observed in the honeycomb compression tests also suggests that the material has limited ductility, which would also contribute to lower tensile elongation and potentially lower UTS compared to a more ductile material. Future tensile testing should employ improved fixturing techniques (e.g., using hydraulic grips or designing specimens with larger fillets at the gauge-grip transition) and meticulous surface preparation in the grip area to minimize stress concentrations and ensure fracture occurs within the gauge length, providing a more accurate assessment of tensile properties.

Figure 18. Fractured Tensile testing samples

Furthermore, the SEM analysis provided crucial insights into the microstructure and defect population within the printed material, revealing the presence of pores and potential microcracks, alongside non-metallic inclusions or precipitates. These defects, particularly microcracks and significant porosity resulting from insufficient melting or gas entrapment, act as potent stress risers under tensile loading and can significantly degrade tensile strength and ductility, even if compressive strength is relatively high. Compressive loading tends to close or be less sensitive to such defects compared to tensile loading, which actively propagates cracks. The presence of these defects, coupled with the off-specification powder composition (which can influence the formation of brittle intermetallic phases or reduce the volume fraction of strengthening precipitates), likely contributed to the overall lower-than-expected tensile performance, independent of the fracture location issue. The observation of linear streaks and branched fragments in the SEM images, potentially representing microcracks, is particularly concerning for tensile performance.

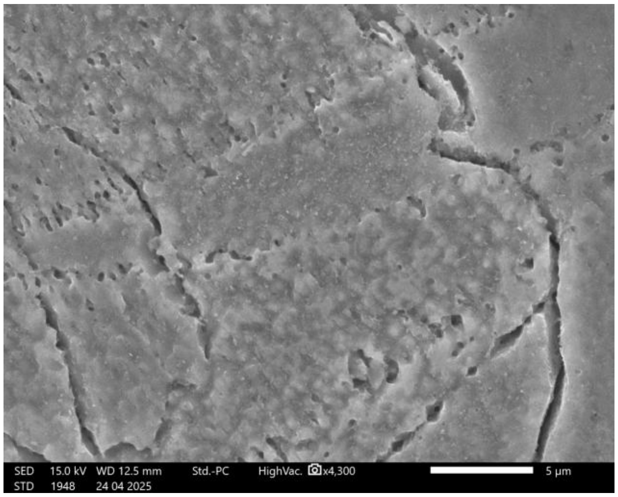

Figure 19. Cracks

Following the optimization of printing parameters based on the mechanical property testing of the different batches, the study proceeded to investigate the energy absorption capabilities of different honeycomb structures fabricated using the optimized Al7075 parameters. The primary objective of this phase was to compare the energy dissipation characteristics of a symmetrical honeycomb design against an asymmetrical 30◦ SSR structure under compressive loading. Energy absorption in cellular structures like honeycombs under compression is primarily related to the area under the stress-strain curve up to the point of densification. This area represents the work done to deform the structure. The symmetrical structure served as a baseline, exhibiting an energy absorption of 39.617 J/m^3. Its energy absorption behavior was likely dominated by a more uniform and predictable buckling response of its constituent hexagonal cells, followed by fracture once the local stresses exceeded the material's brittle fracture strength. In stark contrast, the asymmetrical 30◦ SSR honeycomb demonstrated a notable 8% improvement in energy absorption, reaching 43.036 J/m^3. This enhanced performance in the asymmetrical design is directly attributable to the tailored deformation mechanisms facilitated by the broken symmetry. Unlike symmetrical structures that might undergo sudden, catastrophic global buckling and immediate brittle fracture, asymmetrical designs can promote a more progressive and localized collapse. The re-entrant geometry and asymmetry influence the stress distribution within the cell walls, leading to sequential yielding or fracture of individual cell walls or rows of cells rather than a simultaneous failure across the structure. This controlled, sequential deformation allows the structure to absorb energy more effectively by distributing plastic deformation (even limited, given the brittle nature) and fracture events throughout a larger volume and sustaining significant load over greater displacement before reaching full densification. This aligns with the fundamental principles of mechanical metamaterials, where the macroscopic functional properties, such as energy absorption, are intricately linked to the designed geometry and arrangement of the unit cells [23]. It is important to note that during compression testing, the printed honeycomb structures exhibited brittle fracture behavior rather than significant ductile yielding. This brittle response, characterized by rapid crack initiation and propagation with minimal plastic deformation, inherently limits the amount of energy that can be absorbed through plastic work within the cell walls before catastrophic failure occurs. Despite this inherent brittle characteristic of the Al7075 material processed by SLM, the asymmetrical 30◦ re-entrant angle in the SSR design still proved effective in promoting a more favorable, albeit brittle, collapse mechanism that enhanced energy absorption relative to the symmetrical structure, which also fractured in a brittle manner. The asymmetry likely influenced the stress distribution within the cell walls, leading to a more distributed pattern of crack initiation and propagation rather than a single, rapid failure event across the structure. This more distributed failure mode, involving multiple fracture events occurring sequentially, allowed for greater energy dissipation before complete structural integrity was lost, resulting in the observed improvement in energy absorption. Further investigation into the precise brittle fracture mechanisms and crack propagation paths within the asymmetrical structures through advanced techniques like high-speed imaging and acoustic emission monitoring during compression could provide deeper insights into how the asymmetry influences crack behavior and energy dissipation in this brittle material.

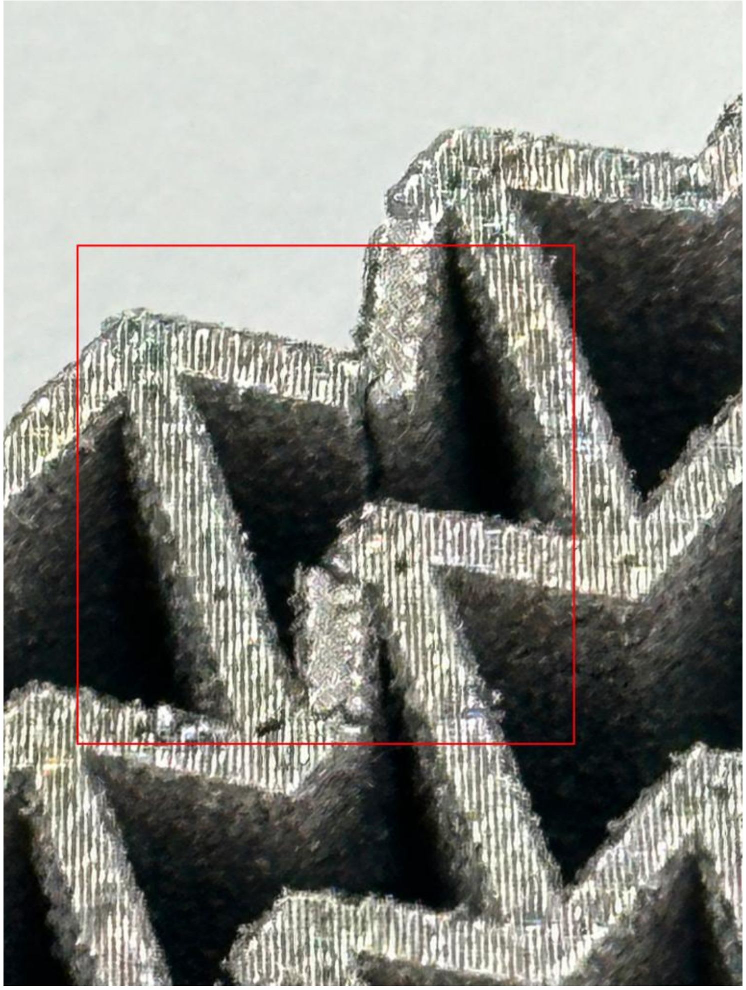

Figure 20. Fractured honeycomb structure

6. Limitations

This study, while providing valuable insights into the SLM processing of Al7075 and the energy absorption of asymmetrical structures, is subject to several limitations that should be acknowledged when interpreting the results and planning future research.

Firstly, the parameter optimization process was limited to a relatively narrow range of adjustments based on an AlSi10Mg baseline. This initial approach was pragmatic given the lack of established parameters for Al7075 on the specific AM400 machine used. However, the optimization involved only incremental increases in laser power and exposure time in a sequential manner. A more comprehensive exploration of the Al7075 process window would ideally involve a designed experiment (e.g., using Design of Experiments methodologies like fractional factorial or response surface methods) to investigate a wider range of parameters, including scan speed, hatch spacing, layer thickness, and potentially scan strategy (e.g., island scanning, stripe scanning). Such an approach could more effectively identify optimal parameter combinations and reveal potential synergistic effects that were not captured by the stepwise adjustments made. This limited exploration means the identified parameters, while showing improvement, may not represent the absolute optimum for achieving the best possible material density, microstructure, and mechanical properties for Al7075 on this platform.

Secondly, the characterization of the Al7075 powder feedstock revealed significant deviations in key alloying element compositions (specifically lower Mg and Zn, and higher Cu) compared to standard specifications for wrought Al7075. The mechanical properties of age-hardenable aluminum alloys like Al7075 are highly dependent on the precise content and ratio of alloying elements, which dictate the formation and effectiveness of strengthening precipitates (primarily MgZn2). This compositional variation inherently impacts the material's metallurgical response during the rapid heating and cooling cycles of SLM, influencing solidification behavior, phase formation, and precipitation hardening kinetics. The mechanical properties obtained in this study are therefore specific to this particular powder batch and may not be directly transferable or representative of results that would be obtained using Al7075 powder from different suppliers or with compositions strictly adhering to standards. This fundamental material variability makes it challenging to definitively isolate the effects of processing parameters from those of the initial material chemistry, potentially confounding the interpretation of the optimization results.

Thirdly, the tensile testing results were significantly affected by premature fracture near the grips, preventing an accurate assessment of the material's true ultimate tensile strength (UTS) and ductility in the gauge section. The observed fracture location suggests that stress concentrations introduced by the gripping mechanism, potential misalignment during testing, or localized weaknesses in the specimen near the grip area (possibly due to surface irregularities from support removal, residual stresses, or a higher concentration of defects in those regions) were the dominant factors leading to failure, rather than the intrinsic tensile strength of the material itself. This issue highlights a significant limitation in the testing methodology employed and means that the tensile data presented should be interpreted with extreme caution as lower-bound estimates. Without reliable tensile data obtained from fractures within the gauge length, a complete understanding of the material's anisotropic mechanical behavior (differences in properties based on build direction, which is crucial for SLM materials) is also limited, impacting the ability to fully characterize the material's suitability for structural applications.

Fourthly, while the study demonstrated the enhanced energy absorption of the asymmetrical structure compared to the symmetrical design, the observed brittle fracture behavior of both types of honeycombs during compression suggests that the material's inherent ductility after SLM and any post-processing is a limiting factor in maximizing energy absorption through plastic deformation. In ductile materials, energy absorption in cellular structures is often dominated by controlled plastic yielding and buckling of cell walls, leading to a plateau region in the stress-strain curve. The brittle response observed here, characterized by rapid crack initiation and propagation with minimal plastic deformation, inherently limits the amount of energy that can be absorbed through plastic work before catastrophic structural failure occurs. The energy absorption in this case is primarily dominated by the energy required for brittle fracture events, which may be less efficient, less predictable, and potentially lower in magnitude compared to energy dissipation through significant plastic deformation in a more ductile material.

Finally, the study focused on evaluating the energy absorption of only one specific type of asymmetrical structure (30∘ SSR honeycomb) and compared it solely to a symmetrical design. Investigating a wider variety of asymmetrical geometries, including different re-entrant angles (e.g., 40∘ SSR as mentioned in the methodology but not explicitly discussed in the results/discussion provided for energy absorption) or other complex metamaterial topologies such as gyroids or Schwarz structures, could provide a more comprehensive understanding of how different types and degrees of structural asymmetry influence energy absorption mechanisms and efficiency in SLM Al7075. Furthermore, the influence of build orientation on the energy absorption behavior of these structures was not explicitly explored. Given the anisotropic nature often observed in SLM parts due to the layer-by-layer process and directional solidification, the orientation of the metamaterial structure relative to the build direction could significantly impact its deformation and energy absorption characteristics.

7. Conclusion

This project successfully investigated the energy absorption capabilities of additively manufactured mechanical metamaterial structures using Al7075 aluminum alloy via Selective Laser Melting (SLM). A key initial step involved optimizing SLM printing parameters for A17075, which is challenging to process due to its susceptibility to cracking. Parameter optimization was performed by systematically adjusting laser power and exposure time, starting from an AlSi10Mg baseline, and evaluating resulting mechanical properties like compressive strength, hardness, and tensile strength. The optimization process successfully improved the compressive strength of the A17075 material.

Following parameter optimization, symmetrical and asymmetrical SSR honeycomb structures were printed and subjected to compression testing to assess their energy absorption performance. The asymmetrical 30º SSR design demonstrated an improved energy absorption capacity compared to the symmetrical structure, although both exhibited brittle fracture behavior under compression.

This project highlights the potential of structural asymmetry in enhancing energy absorption in additively manufactured A17075 metamaterials. It also underscores the importance of robust parameter optimization and addressing material brittleness and testing methodology limitations for high-performance applications like aircraft wing leading edges.

The project’s findings contribute to bridging the gap between theoretical design and practical implementation, unlocking new possibilities for metamaterials in high-performance systems. Future research could explore a wider range of asymmetrical geometries and post-processing techniques to enhance ductility and further improve energy absorption performance

References:

[1]S. Dalela, P. S. Balaji, and D. P. Jena, “A review on application of mechanical metamaterials for vibration control,” Mechanics of Advanced Materials and Structures, pp. 1–26, Feb. 2021, doi: https://doi.org/10.1080/15376494.2021.1892244.

[2]J. Bauer, L. R. Meza, T. A. Schaedler, R. Schwaiger, X. Zheng, and L. Valdevit, “Nanolattices: An Emerging Class of Mechanical Metamaterials,” Advanced Materials, vol. 29, no. 40, pp. 1701850–1701850, Oct. 2017, doi: https://doi.org/10.1002/adma.201701850.

[3]S. Macrae Montgomery et al., “Magneto-Mechanical Metamaterials with Widely Tunable Mechanical Properties and Acoustic Bandgaps,” Advanced Functional Materials, vol. 31, no. 3, Oct. 2020, doi: https://doi.org/10.1002/adfm.202005319.

[4]A. J. D. Shaikeea, H. Cui, M. O’Masta, X. R. Zheng, and V. S. Deshpande, “The toughness of mechanical metamaterials,” Nature Materials, vol. 21, no. 3, pp. 297–304, Feb. 2022, doi: https://doi.org/10.1038/s41563-021-01182-1.

[5]A. Álvarez-Trejo, E. Cuan-Urquizo, D. Bhate, and A. Roman-Flores, “Mechanical metamaterials with topologies based on curved elements: An overview of design, additive manufacturing and mechanical properties,” *Materials & Design*, vol. 233, p. 112190, Sep. 2023, doi: https://doi.org/10.1016/j.matdes.2023.112190.

[6]W. Wu, W. Hu, G. Qian, H. Liao, X. Xu, and F. Berto, “Mechanical design and multifunctional applications of chiral mechanical metamaterials: A review,” Materials & Design, vol. 180, p. 107950, Oct. 2019, doi: https://doi.org/10.1016/j.matdes.2019.107950.

[7]E. Bahmanpour, A. Montazeri, A. Saeedi, and M. Mahnama, “Flexural behaviors of asymmetric re-entrant auxetic honeycombs,” *European Journal of Mechanics - a/Solids*, p. 105475, Oct. 2024, doi: 10.1016/j.euromechsol.2024.105475.

[8]S. Devaganesh, P. K. Dinesh Kumar, N. Venkatesh, and R. Balaji, “Study on the mechanical and tribological performances of hybrid SiC-Al7075 metal matrix composites,” *Journal of Materials Research and Technology*, vol. 9, no. 3, pp. 3759–3766, May 2020, doi: https://doi.org/10.1016/j.jmrt.2020.02.002

[9] G. B. V. Kumar, C. S. P. Rao, and N. Selvaraj, “Mechanical and Tribological Behavior of Particulate Reinforced Aluminum Metal Matrix Composites – a review,” Journal of Minerals and Materials Characterization and Engineering, vol. 10, no. 01, pp. 59–91, 2011, doi: https://doi.org/10.4236/jmmce.2011.101005.

[10]Donik, Č., Kraner, J., Paulin, I., & Godec, M. (2020). Influence of the energy density for selective laser melting on the microstructure and mechanical properties of stainless steel. *Metals*, *10*(7), 919. https://doi.org/10.3390/met10070919

[11]Liu, S., Li, H., Qin, C., Zong, R., & Fang, X. (2020). The effect of energy density on texture and mechanical anisotropy in selective laser melted Inconel 718. *Materials & Design*, *191*, 108642. https://doi.org/10.1016/j.matdes.2020.108642

[12]Ge, J., Yuan, B., Zhao, L., Yan, M., Chen, W., & Zhang, L. (2022). Effect of volume energy density on selective laser melting NiTi shape memory alloys: microstructural evolution, mechanical and functional properties. *Journal of Materials Research and Technology*, *20*, 2872–2888. https://doi.org/10.1016/j.jmrt.2022.08.062

[13]Pechlivani, E. M., Melidis, L., Pemas, S., Katakalos, K., Tzovaras, D., & Konstantinidis, A. A. (2023). On the Effect of Volumetric Energy Density on the Characteristics of 3D-Printed Metals and Alloys. *Metals*, *13*(10), 1776. https://doi.org/10.3390/met13101776

[14]Cui, Y., Cai, J., Li, Z., Jiao, Z., Hu, L., & Hu, J. (2022). Effect of porosity on dynamic response of additive manufacturing TI-6AL-4V alloys. *Micromachines*, *13*(3), 408. https://doi.org/10.3390/mi13030408

[15]Saxena, P., Gajera, H., Shah, D., & Pancholi, N. (2021). Effect of SLM process parameters on hardness and microstructure of stainless steel 316 material. *Materials Today Proceedings*, *50*, 1653–1659. https://doi.org/10.1016/j.matpr.2021.09.144

[16]Khorasani, A., Gibson, I., Awan, U. S., & Ghaderi, A. (2018). The effect of SLM process parameters on density, hardness, tensile strength and surface quality of Ti-6Al-4V. *Additive Manufacturing*, *25*, 176–186. https://doi.org/10.1016/j.addma.2018.09.002

[17]Liang, G., Ali, Y., You, G., & Zhang, M. (2018). Effect of cooling rate on grain refinement of cast aluminium alloys. *Materialia*, *3*, 113–121. https://doi.org/10.1016/j.mtla.2018.08.008

[18]Nakai, R., Yabuuchi, K., Nogami, S., & Hasegawa, A. (2015). The effect of voids on the hardening of body-centered cubic Fe. *Journal of Nuclear Materials*, *471*, 233–238. https://doi.org/10.1016/j.jnucmat.2015.09.048

[19]Lee, H. (2022). Effects of the Energy Density on Pores, Hardness, Surface Roughness, and Tensile Characteristics of Deposited ASTM 316L Specimens with Powder-Bed Fusion Process. *Materials*, *15*(19), 6672. https://doi.org/10.3390/ma15196672

[20]Dobson, S., Vunnam, S., Frankel, D., Sudbrack, C., & Starr, T. (2019, January 1). *Powder variation and mechanical properties for SLM 17-4 PH Stainless steel*. Solid Freeform Fabrication Symposium – an Additive Manufacturing Conference. https://doi.org/10.26153/tsw/17286

[21]Tiscareno, E. G., Taylor, H., Lynch, C., Villalobos, J., & Wicker, R. (2024). Sensitivity of mechanical properties to processing defects: Is tensile testing an appropriate metric for laser beam metal powder bed fusion machine qualification? *Additive Manufacturing*, *93*, 104367. https://doi.org/10.1016/j.addma.2024.104367

[22]Pellizzari, M., AlMangour, B., Benedetti, M., Furlani, S., Grzesiak, D., & Deirmina, F. (2020). Effects of building direction and defect sensitivity on the fatigue behavior of additively manufactured H13 tool steel. *Theoretical and Applied Fracture Mechanics*, *108*, 102634. https://doi.org/10.1016/j.tafmec.2020.102634

[23] Xu, H., Liu, H., & Li, G. (2024). In-plane characteristics of a multi-arc re-entrant auxetic honeycomb with enhanced negative Poisson’s ratio effect and energy absorption. *European Journal of Mechanics - a/Solids*, 105473. https://doi.org/10.1016/j.euromechsol.2024.105473

Appendix A. Printing failures

Figure 1. Failed print #1

Figure 2. Failed print #2

Figure 3. Failed print #3

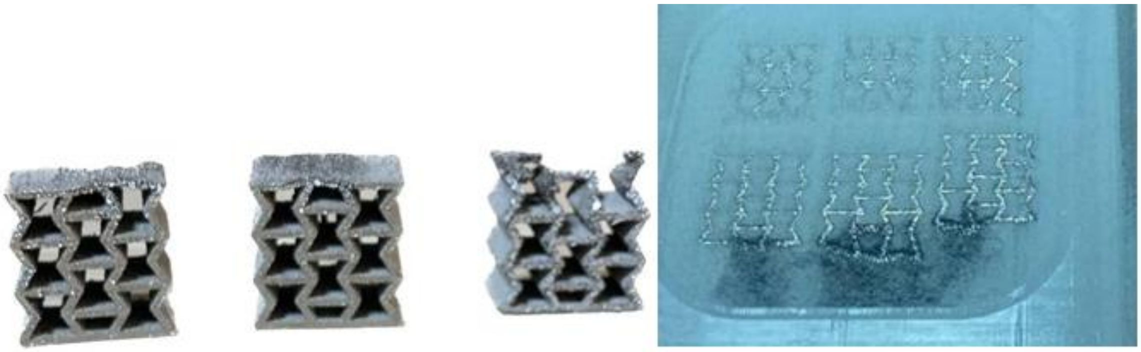

Figure 4. Failed print #4

Appendix B. SEM and EDS

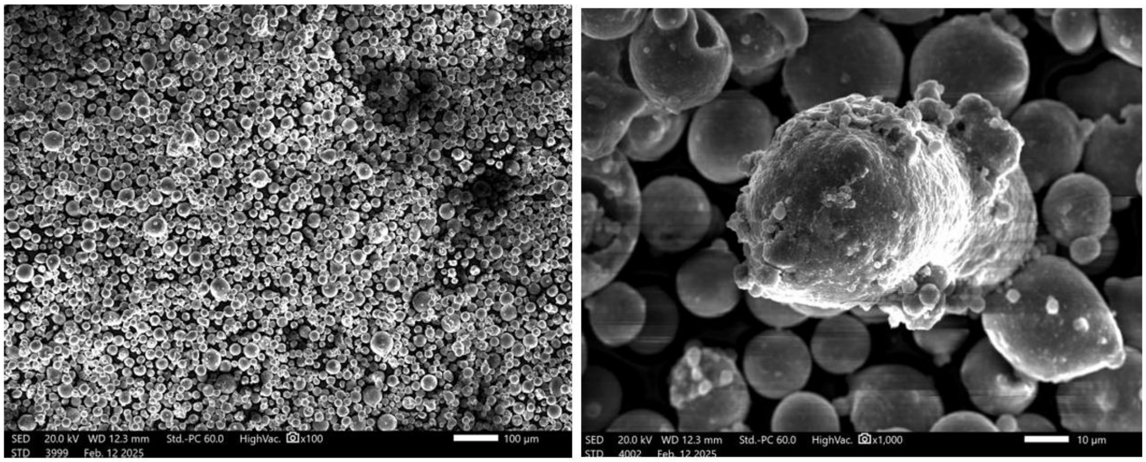

Figure 5. Power SEM

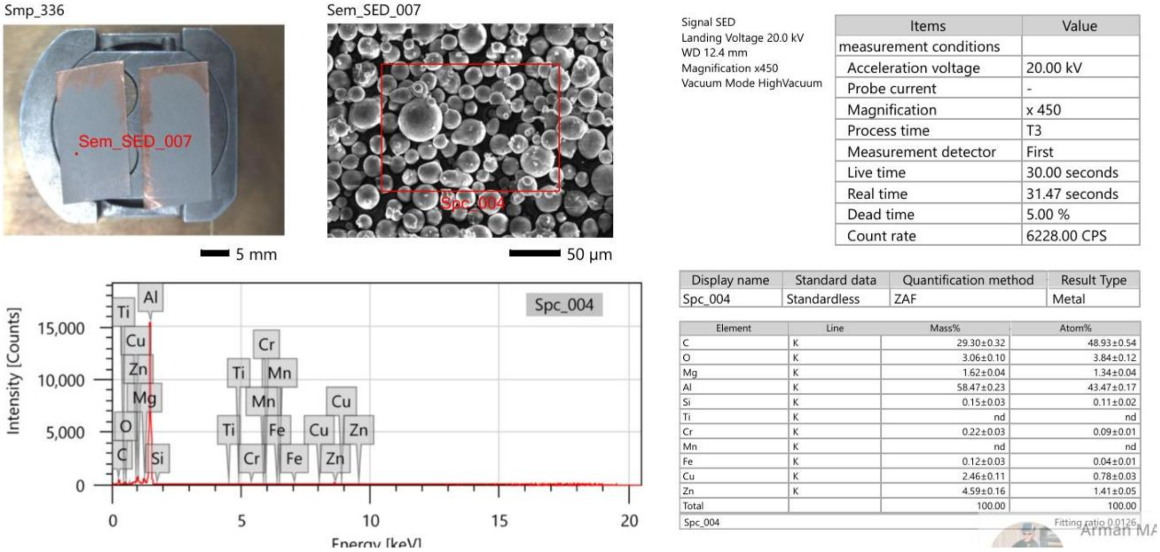

Signal SED
Landing Voltage 20.0 kV
WD 12.4 mm
Magnification x450
Vacuum Mode HighVacuum

Items	Value
measurement conditions	
Acceleration voltage	20.00 kV
Probe current	-
Magnification	x 450
Process time	T3
Measurement detector	First
Live time	30.00 seconds
Real time	31.47 seconds
Dead time	5.00 %
Count rate	6228.00 CPS

Display name	Standard data	Quantification method	Result Type
Spc_004	Standardless	ZAF	Metal

Element	Line		Mass%	Atom%
C	K		29.30±0.32	48.93±0.54
O	K		3.06±0.10	3.84±0.12
Mg	K		1.62±0.04	1.34±0.04
Al	K		58.47±0.23	43.47±0.17
Si	K		0.15±0.03	0.11±0.02
Ti	K		nd	nd
Cr	K		0.22±0.03	0.09±0.01
Mn	K		nd	nd
Fe	K		0.12±0.03	0.04±0.01
Cu	K		2.46±0.11	0.78±0.03
Zn	K		4.59±0.16	1.41±0.05
Total			100.00	100.00

Spc_004 Fitting ratio 0.0126

Figure 6. Powder EDS

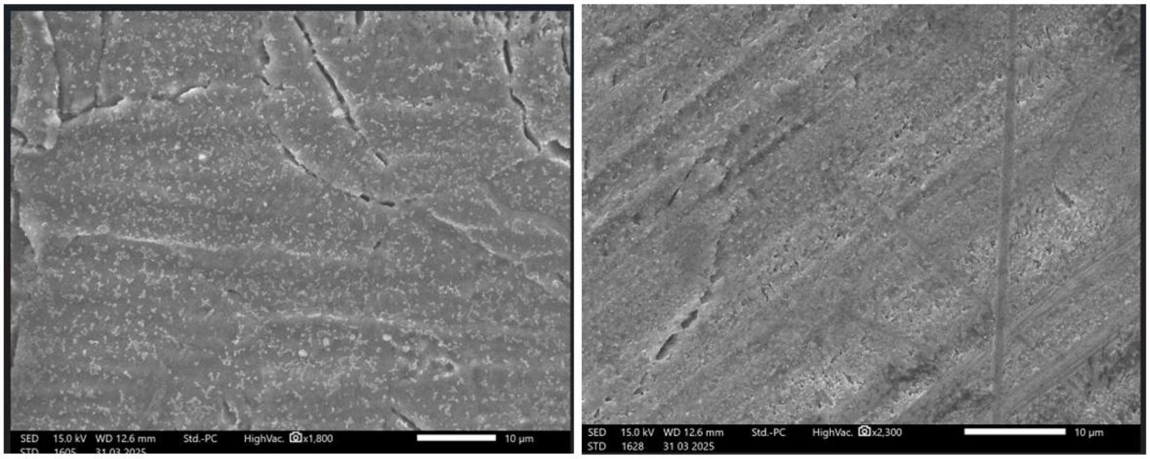

Figure 7. Etching 15min

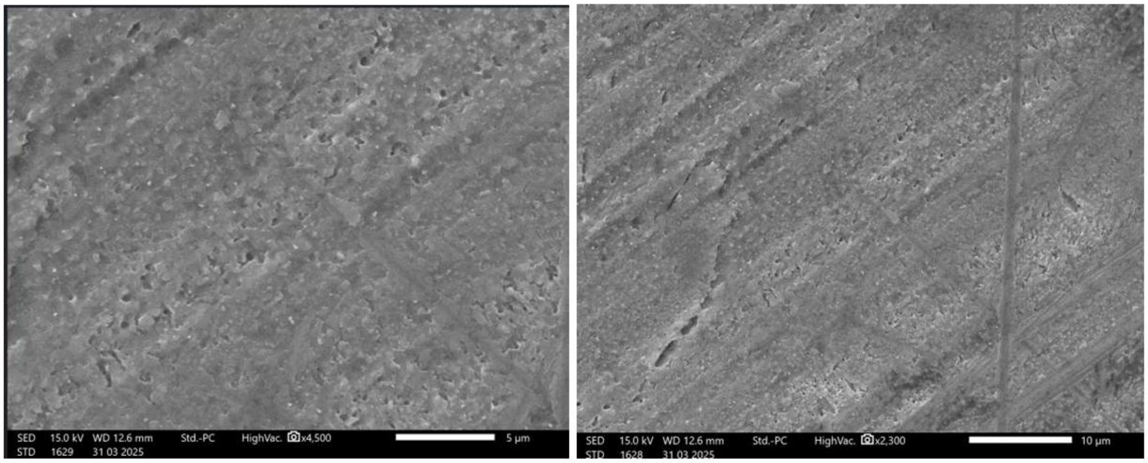

Figure 8. Etching 10min

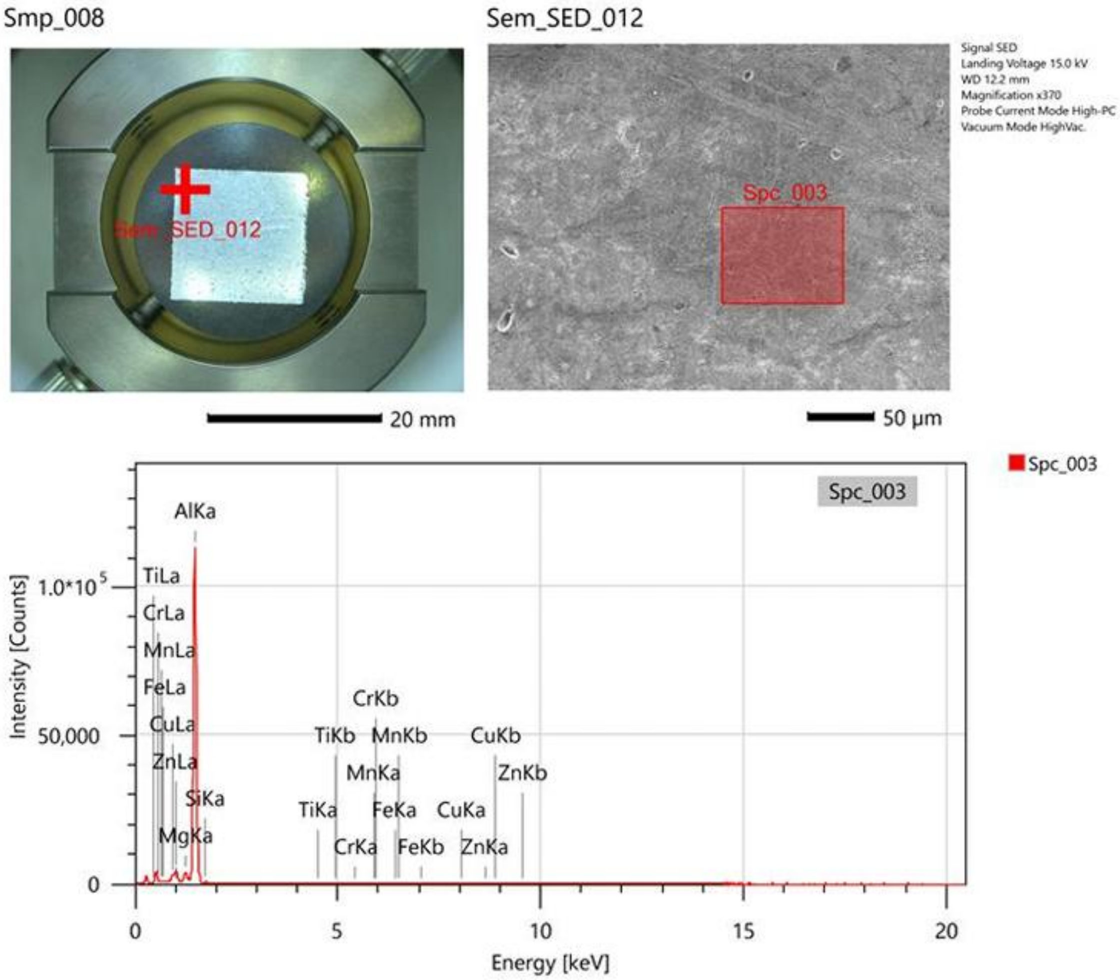

Name	Mg	Al	Si	Ti	Cr	Mn	Fe	Cu	Zn	Total
Spc_003	2.03	90.02	0.51	0.00	0.17	nd	0.15	2.64	4.47	100.00
Average	2.03	90.02	0.51	0.00	0.17	0.00	0.15	2.64	4.47	
Standard Deviation										

Atom/Mol%

Figure 9. EDS of sample

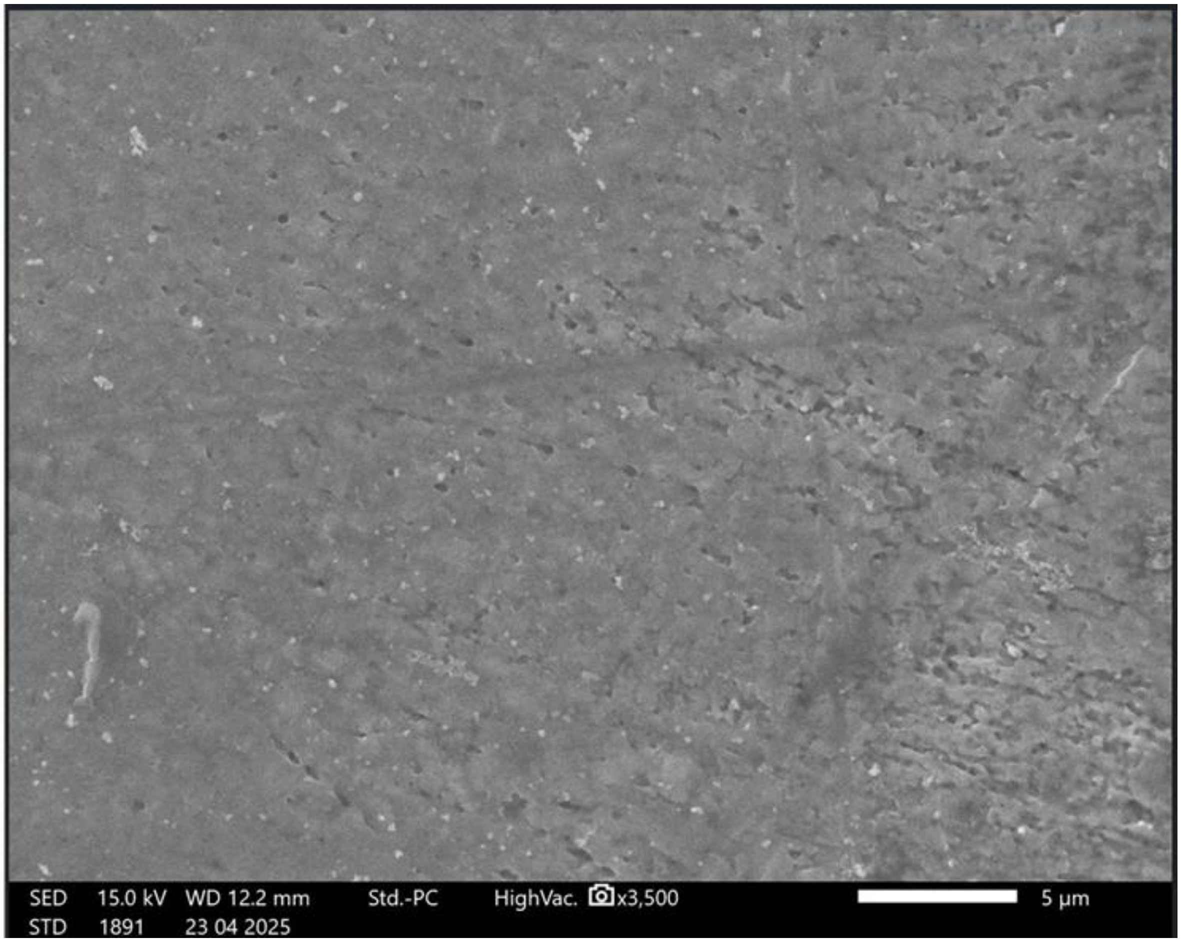

Figure 10. SEM 1 min etching

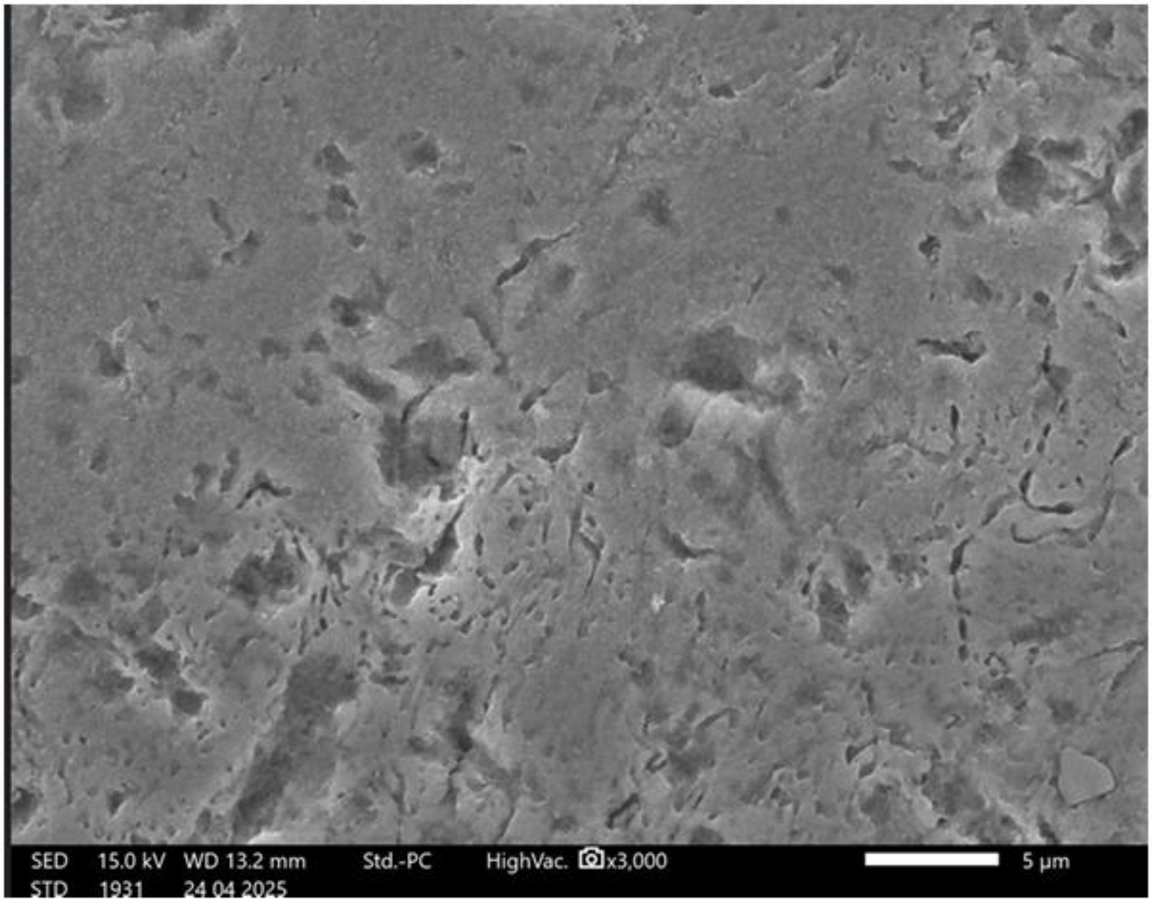

Figure 11. Etching 35 sec

Appendix C. Initial parameters

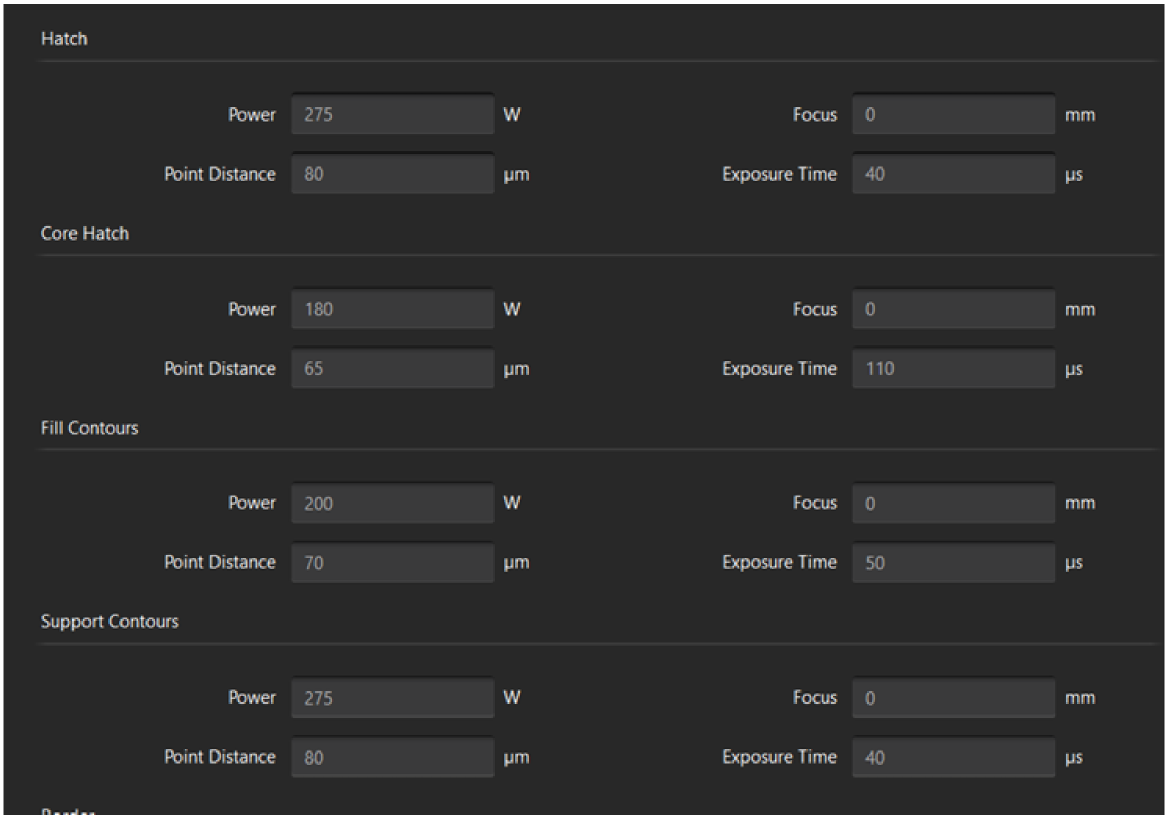

Hatch

Power 275 W
Focus 0 mm
Point Distance 80 µm
Exposure Time 40 µs

Core Hatch

Power 180 W
Focus 0 mm
Point Distance 65 µm
Exposure Time 110 µs

Fill Contours

Power 200 W
Focus 0 mm
Point Distance 70 µm
Exposure Time 50 µs

Support Contours

Power 275 W
Focus 0 mm
Point Distance 80 µm
Exposure Time 40 µs

Figure 12. Initial Parameters